Magnetic domain configuration of (111)-oriented $LaFeO_3$ epitaxial thin films

I. Hallsteinsen, M. Moreau, R. V. Chopdekar, E. Christiansen, M. Nord, P.-E. Vullum, J. K. Grepstad, R. Holmestad, S. M. Selbach, A. Scholl, E. Arenholz, E. Folven, and T. Tybell

Citation: APL Materials **5**, 086107 (2017);
View online: https://doi.org/10.1063/1.4986555
View Table of Contents: http://aip.scitation.org/toc/apm/5/8
Published by the American Institute of Physics

Articles you may be interested in

Interfacial B-site atomic configuration in polar (111) and non-polar (001) $SrIrO_3/SrTiO_3$ heterostructures
APL Materials **5**, 096110 (2017); 10.1063/1.4993170

Modified magnetic anisotropy at $LaCoO_3/La_{0.7}Sr_{0.3}MnO_3$ interfaces
APL Materials **5**, 096104 (2017); 10.1063/1.5002090

Magnetic-coupled phase anomaly in mixed-phase $BiFeO_3$ thin films
APL Materials **5**, 086112 (2017); 10.1063/1.4990138

Effect of gate voltage polarity on the ionic liquid gating behavior of $NdNiO_3/NdGaO_3$ heterostructures
APL Materials **5**, 051101 (2017); 10.1063/1.4983617

Exposing high-energy surfaces by rapid-anneal solid phase epitaxy
APL Materials **5**, 086103 (2017); 10.1063/1.4992004

Fabrication and characterization of abrupt TiO_2–SiO_x core-shell nanowires by a simple heat treatment
APL Materials **5**, 086101 (2017); 10.1063/1.4996211

APL MATERIALS **5**, 086107 (2017)

Magnetic domain configuration of (111)-oriented $LaFeO_3$ epitaxial thin films

I. Hallsteinsen,[1,2] M. Moreau,[1] R. V. Chopdekar,[3] E. Christiansen,[4] M. Nord,[4] P.-E. Vullum,[5] J. K. Grepstad,[1] R. Holmestad,[4] S. M. Selbach,[6] A. Scholl,[2] E. Arenholz,[2] E. Folven,[1] and T. Tybell[1,a]

[1]*Department of Electronic Systems, NTNU–Norwegian University of Science and Technology, Trondheim 7491, Norway*
[2]*Advanced Light Source, Lawrence Berkeley National Laboratory, Berkeley, California 94720, USA*
[3]*Department of Chemical Engineering and Materials Science, University of California, Davis, California 95616, USA*
[4]*Department of Physics, NTNU–Norwegian University of Science and Technology, Trondheim 7491, Norway*
[5]*SINTEF Materials and Chemistry, Trondheim 7491, Norway*
[6]*Department of Materials Science and Engineering, NTNU–Norwegian University of Science and Technology, Trondheim 7491, Norway*

(Received 6 June 2017; accepted 9 August 2017; published online 22 August 2017)

In antiferromagnetic spintronics control of the domains and corresponding spin axis orientation is crucial for devices. Here we investigate the antiferromagnetic axis in (111)-oriented $LaFeO_3/SrTiO_3$, which is coupled to structural twin domains. The structural domains have either the orthorhombic *a*- or *b*-axis along the in-plane $\langle 1\bar{1}0\rangle$ cubic directions of the substrate, and the corresponding magnetic domains have the antiferromagnetic axis in the sample plane. Six degenerate antiferromagnetic axes are found corresponding to the $\langle 1\bar{1}0\rangle$ and $\langle 11\bar{2}\rangle$ in-plane directions. This is in contrast to the biaxial anisotropy in (001)-oriented films and reflects how crystal orientation can be used to control magnetic anisotropy in antiferromagnets. © *2017 Author(s). All article content, except where otherwise noted, is licensed under a Creative Commons Attribution (CC BY) license (http://creativecommons.org/licenses/by/4.0/).*
[http://dx.doi.org/10.1063/1.4986555]

Antiferromagnetic (AF) spintronics technology has recently emerged as a promising avenue for future electronic device technology.[1,2] AF insulators incorporated in devices are robust against external magnetic fields, produce no stray field that could perturb neighboring devices, have ultra-fast magnetization dynamics, and as no moving charges are involved, their power reduction is significant as compared to charge based electronics used today.[3] In current magnetoelectronic device applications, AF layers play a passive but important role, where they typically serve to pin an adjacent ferromagnetic (FM) layer by force of the exchange-bias coupling.[4] However, the AF layer can also be an active component of electronic devices. Recently, Wadley *et al.*[5] demonstrated switching of the AF spin axis by electric current. Further it was shown that the magnetic domain orientation was correlated to the electrical resistance[6] and used in a multilevel memory device.[7] Both exchange-bias and AF dynamics depend on the AF domain structure, hence a detailed understanding of domain formation and possibly domain engineering are both essential for further device development.[1,5,8]

The mechanisms responsible for domain formation in AF materials are not as straightforward as in the case of FM materials, since there is no macroscopic demagnetizing field. Commonly multi domain configurations are observed in AF materials, which are explained in terms of lattice imperfections, such as crystalline twins or dislocations.[9] In magnetic perovskites oxides, there is a strong coupling between crystalline structure and magnetic properties.[10] Engineered distortions of the crystalline structure, e.g., in epitaxial thin films, couple to the magnetic order parameter through magnetoelastic

[a]Author to whom correspondence should be addressed: thomas.tybell@iet.ntnu.no

 © Author(s) 2017

effects and play a key role in the AF domain formation.[11] Bulk $LaFeO_3$ (LFO) is orthorhombic (space group *Pnma* with a = 5.557 Å, b = 5.5652 Å, and c = 7.8542 Å) with the AF easy axis oriented along the crystallographic *a*-axis. The AF domains of LFO thin films epitaxially grown in the pseudocubic (001)-orientation are extensively studied and strongly coupled to structural changes.[9,12] The strong coupling to the lattice makes LFO an ideal model system to investigate manipulation of the AF domain structure. Seo *et al.*[13] showed that different strain states and miscut of the substrate produce different structural domains which are reflected in the AF domains. In addition, new sets of AF easy axes can be found when LFO is coupled to FM materials.[14]

Until recently, research on epitaxial perovskite thin films has been largely focused on pseudocubic (001)-oriented surfaces; however, different surface orientations can be used as a tool for domain engineering. Recently we have shown that the ferromagnetic anisotropy is biaxial for tensile strained $La_{0.7}Sr_{0.3}MnO_3$ films in the (001)-orientation, while it has a weak anisotropy following the trigonal crystal symmetry in (111)-oriented films.[15] The (111)-oriented perovskite lattice has a threefold in-plane rotational symmetry that forms a buckled honeycomb structure resembling that of topological insulators[16] and multiferroic hexagonal manganites,[17] opening up the possibility for emergent electronic and magnetic behavior. In this letter, we investigate the anisotropy of the AF domains of (111)-oriented LFO. It is shown that LFO strained to a (111)-oriented $SrTiO_3$ (STO) surface has six possible orientations of the orthorhombic unit cell and that the AF domains are similar in size and shape to the structural twins. The AF easy axis is shown to be in the plane of the films along six different crystallographic axes, reflecting the symmetry of the (111)-oriented surface.

Epitaxial 20 nm thick LFO films were fabricated on (111)-oriented Nb-doped (0.05%) STO substrates by pulsed laser deposition. The doped substrates were chosen to prevent charging during the local domain imaging with x-rays. Single terminated smooth substrates were prepared by ultrasonic agitation in deionized water at 70 °C, etching in buffered hydrofluoric acid for 45 s and annealing for 1 h at 1050 °C in an oxygen ambient.[18] A KrF excimer laser (λ = 248 nm) with a fluence of ~2 J cm^{-2} and repetition rate 1 Hz was employed to ablate material from a stoichiometric LFO target. The deposition took place in 0.35 mbars of oxygen at 540 °C, with a substrate-to-target separation of 45 mm, consistent with growth conditions with minimal resputtering.[19] After deposition, the films were cooled to room temperature in 100 mbars of oxygen. The growth was monitored *in situ* with reflection high energy electron diffraction (RHEED), and the surface topography was characterized by atomic force microscopy (AFM, Veeco Nanoscope V) showing a smooth, step-and-terrace surface morphology. The crystalline structure was examined with a four-circle, high-resolution x-ray diffractometer (XRD, Bruker D8), showing fully epitaxial films.

In order to investigate the energetics of possible structural twin arrangements, calculations of the phonon spectrum based on density functional theory (DFT) were performed. The Vienna *Ab initio* Simulation Package (VASP)[20] with the Perdew-Burke-Ernzerhof generalized gradient approximation for solids (PBE-sol) functional and[21] a plane wave cutoff energy of 550 eV and the recommended projected augmented wave (PAW)-PBE potentials supplied with VASP for La, Fe, and O were used. Applying the Dudarev method,[22] a Hubbard U potential of 3 and 10 eV was applied to the Fe 3*d* and La 4*f* orbitals, respectively. Phonon calculations were performed with the frozen phonon approach[23] and analyzed with the Phonopy software.[24] To include the effect of strain, the $[1\bar{1}0]$ and $[01\bar{1}]$ in-plane lattice parameters of LFO were fixed to those calculated for STO, while the out-of-plane lattice parameter along the [111]-direction was allowed to relax. We note that the PBEsol functional has a typical absolute error in lattice parameter of 0.019 Å for transition metals compounds compared to experimental values.[21] Our relaxed value for cubic STO is 3.895 Å, as compared to the experimental 3.905 Å, and for the out of-plane LFO parameter, d_{111}, when strained to STO, we obtain 2.289 Å by DFT as compared to the experimental value of 2.279 Å; that is, both are well within the typical error range.

The AF properties were measured by x-ray magnetic linear dichroism (XMLD) at BL. 4.0.2 of the Advanced Light Source (ALS). XMLD provides information on the projection of the AF spin axis along the E-vector of linearly polarized x-rays. Thus, it is possible to obtain the components of the AF spin axis by rotating the sample relative to the incident beam of x-rays. The spectra shown here were measured in total-electron-yield mode by monitoring the sample drain current, across the Fe $L_{2,3}$ edges (700-730 eV), with the x-rays incident at 30° (grazing incidence) and at 90° to the sample surface (normal incidence). The polarization E-vector was varied between s- (in-plane at

grazing incidence) and p-polarization (60° out-of-plane at grazing incidence), where the difference between them results in the XMLD spectra. In order to probe the microscopic response of individual domains, the films were imaged by x-ray photoemission electron microscopy (X-PEEM) combined with XMLD at the Surface/Interface: Microscopy (SIM) beam line at the Swiss Light Source (SLS) (Figs. 2 and 4) and BL 11.0.1 at ALS (Fig. 5). Due to different storage ring operating conditions, the incoming photon flux was a factor of ~14 higher at SLS as compared to ALS. X-PEEM allows spatial mapping of x-ray absorption at the lateral length scale of single magnetic domains. Thus, when combined with XMLD, the AF spin axis of individual AF domains can be determined. The AF XMLD intensity has a $\cos^2\theta$ dependence, where θ is the angle between the E-vector and the AF spin axis. Therefore, the image contrast is strongest between AF domains with the spin axis parallel and perpendicular to the E-vector. The XMLD-PEEM images presented are obtained by taking the signal ratio between images recorded at the Fe L_{2A} (722.15 eV) and Fe L_{2B} (724.0 eV) peaks, for a given polarization. This procedure removes contributions from the surface topography and enhances the AF contrast. The inclination with the film surface of the incident x-rays was 16° at SLS and 30° at ALS, and all measurements were done at room temperature. The spectra are shown without any attempt to correct for saturation effects, as it does not affect the qualitative interpretation.[25,26]

Figure 1(a) shows the x-ray absorption spectra obtained with s- and p-polarization and the resulting XMLD spectrum at grazing incidence. A clear dichroism signal is obtained, indicating AF order. Through comparison with modeled spectra,[27] the sign of the dichroism indicates an in-plane AF axis. We note that spectra taken at normal incidence with s- and p-polarization (not shown) corresponding to the $[1\bar{1}0]$ and $[11\bar{2}]$ in plane directions, respectively, give almost no dichroism. Hence, the magnetic AF response is similar for the two crystallographic axes, and the structural linear dichroism is negligible. In Fig. 1(b), the XMLD spectra recorded while rotating the sample relative to the incoming x-rays at grazing incidence are shown. The in-plane azimuthal rotation is defined to be $\varphi = 0°$ when the incoming x-ray projection on the film plane is parallel to $[1\bar{1}0]$ and $\varphi = 90°$ when parallel to the $[11\bar{2}]$ crystallographic direction. The magnitude of the dichroism is approximately the same for all angles. With an x-ray spot size of ~100 μm × 100 μm, we are averaging over many domains with different spin axes. The clear dichroism in Fig. 1(b) points towards in-plane

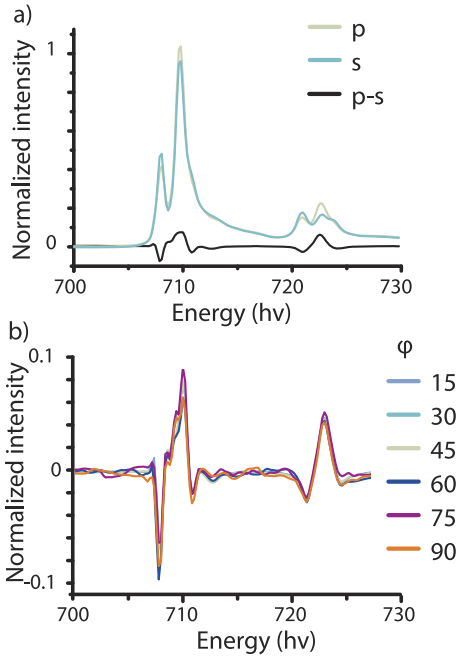

FIG. 1. (a) X-ray absorption spectra of the Fe $L_{2,3}$-edge (700-730 eV) in grazing incidence with polarization p (green) and s (turquoise) and their difference spectrum (black). (b) X-ray linear dichroism spectra of the Fe $L_{2,3}$-edge in grazing incidence upon sample rotation from $\omega = 15°$ to 90°, where $\omega = 0°$ refers to the in-plane projection of x-rays incident parallel to the $[1\bar{1}0]$ cubic substrate crystallographic direction.

AF spin axes; however, the lack of difference as a function of the azimuth angle indicates that we are averaging over domains with many different in-plane directions of the AF spin axes.

To further investigate a possible AF anisotropy and domain structure, we used XMLD - PEEM in the measurement geometry presented in Fig. 2. In the first panel ($\omega = 0°$), a PEEM image recorded with s-polarization is presented. There is clear contrast from different regions, indicative of domains with different AF axis orientation. The domains are irregularly shaped and their size varies between 50 and 500 nm in diameter. Earlier results on similar pseudocubic (001)-oriented films show similar sizes and shapes.[13] In a thin film grown on (001)-oriented $SrTiO_3$ (STO), the orthorhombic *a* axis is pointing 45° out-of-plane, along the cubic ⟨110⟩ axes ($[100]_o$ || $[110]_c$). The AF easy axis was reported to vary from canting angles of 35° to totally in-plane along the two ⟨100⟩ directions.[25,28] If the same crystallographic relation is preserved in a (111)-oriented film, the orthorhombic *a*-axis could either lie in-plane or lie at 55° out-of-plane, aligned with the $\langle 1\bar{1}0 \rangle$ directions. To investigate if the AF spin axes are mainly in-plane or out-of-plane, we varied the polarization from $\omega = 0°$ (s-polarization) to $\omega = 90°$ (p-polarization) in increments of 10°, with incoming light at 16° from the plane of the film. In Fig. 2 the PEEM images recorded for the different polarizations are shown. It is clear that the contrast between the domains decreases as the linear polarization rotates out-of-plane and disappears almost entirely at $\omega = 90°$, indicating that the sensitivity to the AF spin axis of these domains is reduced. The difference between the domains gradually decreases, without any domains emerging stronger at specific angles, demonstrating that the AF axes of the domains lie in the film plane. The same experiment was also executed for azimuthal rotation of $\varphi = 45°$ and 90° (not shown). The results were similar; domain contrast disappears gradually as the polarization is rotated out-of-plane. Hence, we conclude that the domain contrast comes from different in-plane AF spin axes, without any out-of-plane components. This is consistent with data published for (111)-oriented $La_{0.7}Sr_{0.3}FeO_3/La_{0.7}Sr_{0.3}MnO_3$ superlattices, for which the AF spin axis of $La_{0.7}Sr_{0.3}FeO_3$ was found to lie in the film plane for $La_{0.7}Sr_{0.3}FeO_3$ layers thicker than 3.6 nm.[29]

For a (001)-oriented LFO/STO film, the orthorhombic *c* axis can orient itself along both the $[001]_c$ and $[010]_c$ substrate axes [Fig. 3(a)], resulting in structural twinning domains which are directly coupled to the antiferromagnetic domains that lead to biaxial anisotropy.[13] We have recently shown three structural domain variants in a 20 nm thick (111)-oriented LFO thin film by dark field transmission electron microscopy.[30] The structural domains have irregular shape and diameters ranging from 50 to 300 nm. This is comparable to the antiferromagnetic domain sizes, which have similar irregular shape and with sizes of 50–500 nm. It should be noted that the smallest AF domains approach the resolution of the PEEM images. The structural domains differ by having the orthorhombic *a* or *b*

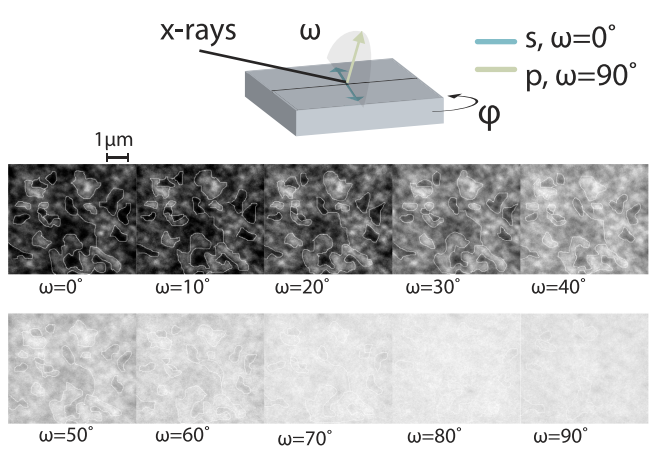

FIG. 2. Schematic of the measurement geometry for PEEM measurements, ω is the x-ray polarization angle with the x-ray polarization axis at $\omega = 0°$ parallel to the sample surface (s-polarization) and φ is the azimuthal sample rotation angle with $\varphi = 0°$ parallel to the cubic $[1\bar{1}0]$ substrate crystallographic direction. PEEM images recorded at $\varphi = 0°$, $\omega = 0° - 90°$ with the outline of some domains drawn in white, showing how the contrast disappears gradually as the polarization is rotated out-of-plane, indicating an in-plane AF spin axis.

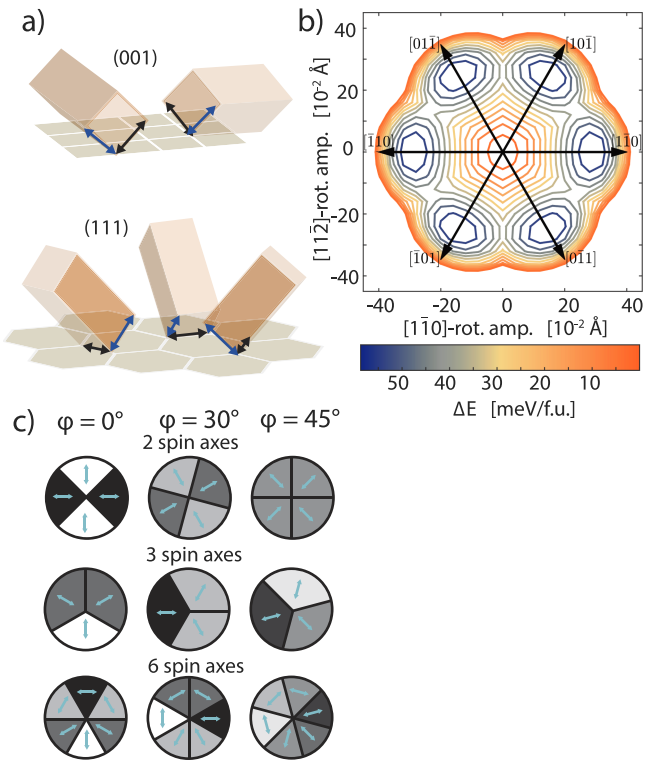

FIG. 3. (a) Schematic of structural domains in the (001) orientation and (111) orientation, with the orthorhombic *a* axis in black and the orthorhombic *b* axis in blue. (b) Energy contour plot for out-of-phase octahedral rotation mode amplitude from DFT calculations for (111)-oriented LFO/STO, showing six minima corresponding to six possible structural domains. (c) Schematic of how different number of spin axis would result in different number of contrast levels for different azimuthal angles (φ = 0°, 30°, and 45°) for polarization parallel to the sample surface (ω = 0°).

lattice parameters oriented parallel to the substrates [1$\bar{1}$0], [$\bar{1}$01], or [0$\bar{1}$1] cubic directions [Fig. 3(a)]. However, as the film is strained to a cubic substrate, it is not possible to distinguish the *a* and *b* lattice parameters; thus, there are effectively six structural variants with equivalent energies. To test this, DFT calculations of the energy landscape as a function of octahedral rotation pattern when LFO is strained to (111)-oriented STO are shown in Fig. 3(b). Bulk LFO has an $a^-a^-c^+$ tilt pattern, corresponding to out-of-phase octahedral rotations around the orthorhombic *a* and *b* axes and in-phase rotation along the c axis. The contour plot in Fig. 3(b) depicts the out-of-phase octahedral rotation mode amplitude around the in-plane directions of the STO substrates, with a constant in-phase rotation amplitude of 0.3 Å. Six discrete energy minima are found, corresponding to out-of-phase octahedral rotation around the ⟨1$\bar{1}$0⟩ directions with an in-phase octahedral rotation around the ⟨100⟩ family. Hence, DFT points towards six possible structural variants for the (111)-oriented LFO/STO system.

In Fig. 3(a) the black arrows indicate the bulk AF spin axis, with a 3-fold AF anisotropy, along the ⟨1$\bar{1}$0⟩ crystalline directions, while the blue arrows indicate the b-axis, which would have an in-plane component along the ⟨11$\bar{2}$⟩ crystal directions. To experimentally determine the in-plane directions of the AF spin axes of the epitaxially strained film, the sample was rotated azimuthally around its center position (φ) and imaged with s-polarized x-rays (ω = 0°). Figure 3(c) depicts a schematic of how different domain structures would look like in PEEM for different azimuthal angles. For (001)-oriented films the AF spin orientation is biaxial, with 90° between the spin axes, resulting in black/white domains at φ = 0°/90° and no domain contrast at φ = 45°, whereas multiple shades of grey are expected for three and six AF spin axes. In Fig. 4, we show corresponding data taken at an azimuthal angle of φ = 0°, 45°, and 90°. The images are shown at the same contrast settings. A similar domain contrast is observed for φ = 45° as for φ = 0° and 90°, clearly suggesting the presence of more than two spin axes. To establish the spin axes, we follow specific domains at different azimuthal angles (φ). In Fig. 4, the high-contrast domains at φ = 0° and 90° are clearly visible. For

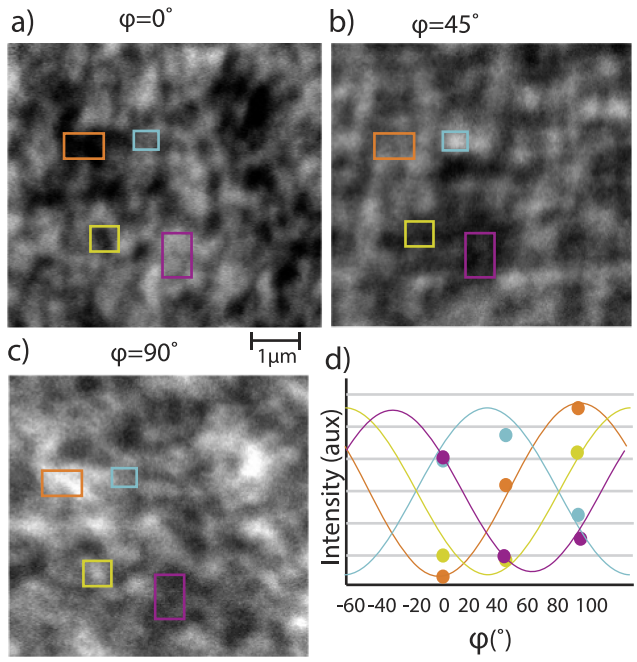

FIG. 4. [(a), (b), and (c)] PEEM images recorded at $\varphi = 0°$, 45°, and 90° and $\omega = 0°$ where $\varphi = 0°$ is parallel to the cubic $[1\bar{1}0]$ substrate crystallographic direction. (d) The average XMLD signal intensity of 4 different domains [indicated in 4(a), (b), and (c) as colored squares] as a function of the azimuthal angle. The expected $\cos^2\theta$ dependence is outlined as a guide to the eye.

data taken at $\varphi = 45°$, the previous black/white domains become grey, and new domains become evident making it difficult to determine the shape of the domains. Figure 4(d) depicts the variation in signal intensity for four domains which are dark and bright in the PEEM image recorded for $\varphi = 0°$. The originally darkest domain in the $\varphi = 0°$ image (orange square) becomes grey for $\varphi = 45°$ and bright for $\varphi = 90°$, in agreement with the AF axis parallel to $\varphi = 90°$. However, for the bright domains in the $\varphi = 0°$ image (turquoise and purple square), one becomes dark (purple) at $\varphi = 45°$, while the other becomes brighter (turquoise), before both domains turn to dark grey in the $\varphi = 90°$ image. The grey domain in $\varphi = 0°$ (yellow) continues to be dark grey in $\varphi = 45°$ and turns bright in $\varphi = 90°$. As a guide to the eye, the expected $\cos^2\theta$ dependence of AF domains with maximum signal intensity at $\varphi = 30°$ (turquoise), 90° (orange), 120° (yellow), and 150° (purple) is plotted in Fig. 4(d). Though only three azimuthal angles are probed, the data fit well with this model and point towards the presence of AF domains with their axes oriented along both the in-plane $\langle 1\bar{1}0\rangle$ and $\langle 11\bar{2}\rangle$ crystallographic directions.

To better probe if an AF spin axis can be oriented along the in-plane $\langle 11\bar{2}\rangle$ direction, a series of images was measured with azimuthal orientation of the sample at $\varphi = 0°$–132°, incremented with 12° per image. The images were then rotated to spatially comply with each other, and principal component analysis (PCA) on the image series was carried out to obtain the azimuthal dependence of the XMLD signal. Different domain categories were defined by having a maximum at a specific angle and a minimum 90° from the maximum, following the $\cos^2\theta$ dependence. In Fig. 5(a) the PEEM image recorded for $\varphi = 0°$ is presented for comparison with the resulting domain categories depicted in different colors in Fig. 5(b). Five different categories are identified, with maxima at $\varphi = 0°$ (blue), 30° (turquoise), 60° (green), 90° (orange), and 120° (yellow). Categories with maxima in between these angles are colored grey. For the images in Fig. 5(a), the spatial resolution is ~100 nm. A good fit between Figs. 5(a) and 5(b) is found with domain features from 100 to 500 nm for all the domain categories. In Fig. 5(c) the mean intensity for the pixels in each category is plotted as a function of azimuthal rotation. A reasonable fit to the expected $\cos^2\theta$ dependence is found for all the five domain categories. Hence, we conclude that all five domain categories are present. In Fig. 5(b) it is clear that the domain categories with maxima at $\varphi = 0°$ (blue), 60° (green), and 90° (orange) are

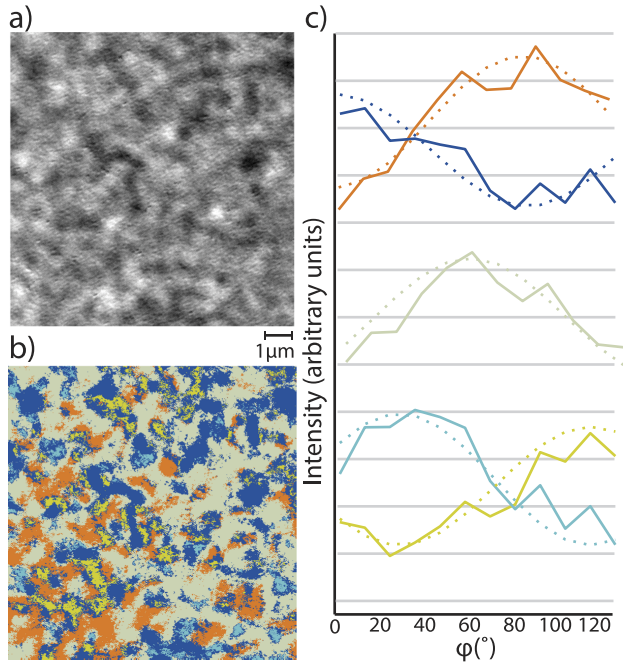

FIG. 5. (a) PEEM image at $\varphi = 90°$ and $\omega = 0°$. (b) A compiled image of the different domain types (colored) found from a stack of PEEM images at $\varphi = 0°–132°$ and $\omega = 0°$, where $\varphi = 0°$ is parallel to the cubic $[1\bar{1}0]$ substrate crystallographic direction. (c) The mean intensity of the pixels for each azimuthal angle categorized by domain type, where blue (orange) has a maximum (minimum) at $\varphi = 0°$, green has a maximum at $\varphi = 60°$, and turquoise (yellow) has a maximum (minimum) at $\varphi = 30°$. With fits of $\cos^2\theta$ dependence as dotted lines.

more dominant than domain categories with maxima at $\varphi = 30°$ (turquoise) and 120° (yellow), and no domains are found with maxima at $\varphi = 150°$ for these images. The orange, turquoise, and missing angle are domains with the AF spin axis along the $\langle 1\bar{1}0\rangle$ family of crystallographic directions, while the blue, green, and yellow are along the $\langle 11\bar{2}\rangle$ family. The difference in dominance does not seem related to crystallographic families and could be due to a random distribution at this specific area of the sample. In Fig. 4 we have indications of domains with maxima at $\varphi = 30°$ (turquoise), 90° (orange), 120° (yellow), and 150° (purple). Taking the data in Figs. 4 and 5 together clearly suggests six possible AF axes in the sample.

In summary, the data reveal that LFO strained to (111)-oriented STO has six possible structural variants, which couple to the AF domain structure. The AF axis is oriented along the in-plane direction of the film, with an energy degeneracy between the $\langle 1\bar{1}0\rangle$ and the $\langle 11\bar{2}\rangle$ in-plane directions, resulting in six possible AF spin axes in for the LFO/STO (111) epitaxial system. The correlation between the AF and structural twin domains, with the orthorhombic *a* and b axes orienting along the ⟨110⟩ cubic substrate axes, opens up the possibility to engineering specific structural domain orientations as a possible avenue to control AF domains in thin films of perovskites.

Part of this work was performed at the SIM beamline of the Swiss Light Source, Paul Scherrer-Institut, Villigen, Switzerland. We thank Michele Buzzi, Dr. Armin Kleibert, and Professor Frithjof Nolting for their assistance with the PEEM experiments. The Advanced Light Source is supported by the Director, Office of Science, Office of Basic Energy Sciences, of the U.S. Department of Energy under Contract No. DE-AC02-05CH11231. Partial funding for these experiments was obtained from Nano-Network under Grant No. 190086/s10 and the Norway America foundation, through Norway House Foundation fund. The Norwegian Metacenter for Computational Science is acknowledged for providing computational resources Uninett Sigma 2, Project No. NN9301K.

[1] T. Jungwirth, X. Marti, P. Wadley, and J. Wunderlich, Nat. Nanotechnol. **11**(3), 231 (2016).
[2] V. Baltz, A. Manchon, M. Tsoi, T. Moriyama, T. Ono, and Y. Tserkovnyak, "Antiferromagnetic spintronics," arXiv:1606.04284 [cond-mat.mtrl-sci].

[3] X. Martí, I. Fina, and T. Jungwirth, IEEE Trans. Magn. **51**(4), 2900104 (2015); E. V. Gomonay and V. M. Loktev, Low Temp. Phys. **40**(1), 17 (2014).
[4] J. Nogués and I. K. Schuller, J. Magn. Magn. Mater. **192**(2), 203 (1999); A. Berkowitz and K. Takano, *ibid.* **200**(1), 552 (1999); M. Kiwi, *ibid.* **234**(3), 584 (2001).
[5] P. Wadley, B. Howells, J. Železný, C. Andrews, V. Hills, R. P. Campion, V. Novák, K. Olejník, F. Maccherozzi, S. S. Dhesi, S. Y. Martin, T. Wagner, J. Wunderlich, F. Freimuth, Y. Mokrousov, J. Kuneš, J. S. Chauhan, M. J. Grzybowski, A. W. Rushforth, K. W. Edmonds, B. L. Gallagher, and T. Jungwirth, Science **351**(6273), 587 (2016).
[6] M. J. Grzybowski, P. Wadley, K. W. Edmonds, R. Beardsley, V. Hills, R. P. Campion, B. L. Gallagher, J. S. Chauhan, V. Novak, T. Jungwirth, F. Maccherozzi, and S. S. Dhesi, Phys. Rev. Lett. **118**(5), 057701 (2017).
[7] K. Olejník, V. Schuler, X. Marti, V. Novák, Z. Kašpar, P. Wadley, R. P. Campion, K. W. Edmonds, B. L. Gallagher, J. Garces, M. Baumgartner, P. Gambardella, and T. Jungwirth, Nat. Commun. **8**, 15434 (2017).
[8] E. G. Tveten, A. Qaiumzadeh, and A. Brataas, Phys. Rev. Lett. **112**(14), 147204 (2014).
[9] A. Scholl, J. Stöhr, J. Lüning, J. W. Seo, J. Fompeyrine, H. Siegwart, J.-P. Locquet, F. Nolting, S. Anders, E. E. Fullerton, M. R. Scheinfein, and H. A. Padmore, Science **287**(5455), 1014 (2000).
[10] H. Y. Hwang, Y. Iwasa, M. Kawasaki, B. Keimer, N. Nagaosa, and Y. Tokura, Nat. Mater. **11**(2), 103 (2012).
[11] E. V. Gomonay and V. M. Loktev, Low Temp. Phys. **30**(10), 804 (2004).
[12] E. Folven, A. Scholl, A. Young, S. T. Retterer, J. E. Boschker, T. Tybell, Y. Takamura, and J. K. Grepstad, Phys. Rev. B **84**(22), 220410 (2011).
[13] J. W. Seo, E. E. Fullerton, F. Nolting, A. Scholl, J. Fompeyrine, and J.-P. Locquet, J. Phys.: Condens. Matter **20**(26), 264014 (2008).
[14] E. Folven, Y. Takamura, and J. K. Grepstad, J. Electron Spectrosc. Relat. Phenom. **185**(10), 381 (2012).
[15] I. Hallsteinsen, E. Folven, F. K. Olsen, R. V. Chopdekar, M. S. Rzchowski, C. B. Eom, J. K. Grepstad, and T. Tybell, APL Mater. **3**(6), 062501 (2015).
[16] X. Liu, S. Middey, Y. Cao, M. Kareev, and J. Chakhalian, MRS Commun. **6**, 133 (2016).
[17] S. M. Griffin, M. Lilienblum, K. T. Delaney, Y. Kumagai, M. Fiebig, and N. A. Spaldin, Phys. Rev. X **2**(4), 041022 (2012).
[18] I. Hallsteinsen, M. Nord, T. Bolstad, P.-E. Vullum, J. E. Boschker, P. Longo, R. Takahashi, R. Holmestad, M. Lippmaa, and T. Tybell, Cryst. Growth Des. **16**(4), 2357 (2016).
[19] I. Hallsteinsen, J. E. Boschker, M. Nord, S. Lee, M. Rzchowski, P. E. Vullum, J. K. Grepstad, R. Holmestad, C. B. Eom, and T. Tybell, J. Appl. Phys. **113**(18), 183512 (2013).
[20] G. Kresse and J. Furthmüller, Phys. Rev. B **54**(16), 11169 (1996); G. Kresse and D. Joubert, *ibid.* **59**(3), 1758 (1999).
[21] J. P. Perdew, A. Ruzsinszky, G. I. Csonka, O. A. Vydrov, G. E. Scuseria, L. A. Constantin, X. Zhou, and K. Burke, Phys. Rev. Lett. **100**(13), 136406 (2008).
[22] S. L. Dudarev, G. A. Botton, S. Y. Savrasov, C. J. Humphreys, and A. P. Sutton, Phys. Rev. B **57**(3), 1505 (1998).
[23] K. Kunc and R. M. Martin, Phys. Rev. Lett. **48**(6), 406 (1982).
[24] M. Moreau, A. Marthinsen, S. M. Selbach, and T. Tybell, Phys. Rev. B **95**(6), 064109 (2017); A. Togo and I. Tanaka, Scr. Mater. **108**, 1 (2015).
[25] J. Lüning, F. Nolting, A. Scholl, H. Ohldag, J. W. Seo, J. Fompeyrine, J.-P. Locquet, and J. Stöhr, Phys. Rev. B **67**(21), 214433 (2003).
[26] R. Nakajima, J. Stöhr, and Y. U. Idzerda, Phys. Rev. B **59**(9), 6421 (1999).
[27] E. Arenholz, G. van der Laan, R. V. Chopdekar, and Y. Suzuki, Phys. Rev. B **74**(9), 094407 (2006); Y. Takamura, F. Yang, N. Kemik, E. Arenholz, M. D. Biegalski, and H. M. Christen, *ibid.* **80**(18), 180417 (2009).
[28] E. Folven, T. Tybell, A. Scholl, A. Young, S. T. Retterer, Y. Takamura, and J. K. Grepstad, Nano Lett. **10**(11), 4578 (2010); F. Nolting, A. Scholl, J. Stohr, J. W. Seo, J. Fompeyrine, H. Siegwart, J. P. Locquet, S. Anders, J. Luning, E. E. Fullerton, M. F. Toney, M. R. Scheinfein, and H. A. Padmore, Nature **405**(6788), 767 (2000); S. Czekaj, F. Nolting, L. J. Heyderman, P. R. Willmott, and G. van der Laan, Phys. Rev. B **73**(2), 020401 (2006).
[29] Y. Jia, R. V. Chopdekar, E. Arenholz, A. T. Young, M. A. Marcus, A. Mehta, and Y. Takamura, Phys. Rev. B **92**(9), 094407 (2015); Y. Jia, R. V. Chopdekar, E. Arenholz, Z. Liu, M. D. Biegalski, Z. D. Porter, A. Mehta, and Y. Takamura, *ibid.* **93**(10), 104403 (2016).
[30] E. Christiansen, M. Nord, I. Hallsteinsen, P. E. Vullum, T. Tybell, and R. Holmestad, J. Phys.: Conf. Ser. **644**(1), 012002 (2015).